Spatial variations in surface sediment structure in riffle-pool sequences: a preliminary test of the Differential Sediment Entrainment Hypothesis (DSEH)

R. A. Hodge[1], D. A. Sear[2], J. Leyland[2]

[1] Department of Geography, Durham University, Science Laboratories, South Road, Durham, DH1 3LE. Email: rebecca.hodge@durham.ac.uk.

[2] Geography and Environment, University of Southampton, Highfield, Southampton, SO17 1BJ UK; Email: D.Sear@soton.ac.uk; J.Leyland@soton.ac.uk

Abstract

Riffle-pool sequences are maintained through the preferential entrainment of sediment grains from pools rather than riffles. This preferential entrainment has been attributed to a reversal in the magnitude of velocity and shear stress under high flows; however the Differential Sediment Entrainment Hypothesis (DSEH) postulates that differential entrainment can instead result from spatial sedimentological contrasts. Here we use a novel suite of *in-situ* grain-scale field measurements from a riffle-pool sequence to parameterise a physically-based model of grain entrainment. Field measurements include pivoting angles, lift forces and high resolution DEMs acquired using Terrestrial Laser Scanning, from which particle exposure, protrusion and surface roughness were derived. The entrainment model results show that grains in pools have a lower critical entrainment shear stress than grains in either pool exits or riffles. This is because pool grains have looser packing, hence greater exposure and lower pivoting angles. Conversely, riffle and pool exit grains have denser packing, lower exposure and higher pivoting angles. A cohesive matrix further stabilises pool exit grains. The resulting predictions of critical entrainment shear stress for grains in different subunits are compared with spatial patterns of bed shear stress derived from a 2D Computational Fluid Dynamics (CFD) model of the reach. The CFD model predicts that, under bankfull conditions, pools experience lower shear stresses than riffles and pool exits. However, the difference in sediment entrainment shear stress is sufficiently large that sediment in pools is still more likely to be entrained than sediment in pool exits or riffles, resulting in differential entrainment under bankfull flows. Significantly, this differential entrainment does not require a reversal in flow velocities or shear stress, suggesting that sedimentological contrasts alone may be sufficient for the maintenance of riffle-pool sequences. This finding has implications

for the prediction of sediment transport and the morphological evolution of gravel-bed rivers.

Keywords

Entrainment, Sediment packing, Riffle-pool, Terrestrial Laser Scanning, Bed shear stress,

1. Introduction and theory

The surface of gravel-bed rivers represents an important control on flow resistance (Smart *et al.*, 2004), boundary layer dynamics (Buffin-Belanger *et al.*, 2006), and the entrainment and transport of bed material (Hodge *et al.*, 2007). Gravel surfaces are also the interface between bulk channel flow and shallow hyporheic flows (Harvey and Bencala, 1993), control the infiltration of fine sediments into the bed (Frostick *et al.*, 1984; Sear *et al.*, 2008), and provide a substrate for a range of biota (Johnson *et al.*, 2009; Johnson *et al.*, 2010; Jones *et al.*, 2011; Kemp *et al.*, 2011).

Much research has explored the spatial and temporal distribution of particle sizes at the bed surface; however, sediment size alone cannot fully explain the dynamics of sediment transport in alluvial rivers. It is likely that the structural arrangement of particles plays a critical role in causing variability in sediment transport (Jerolmack, 2011). Flowing water organises particles into structural groups and bed fabrics; surface particles are repositioned into more stable positions within the bed by small *in-situ* particle movements during periods of sub-critical and turbulent flows (Clifford and Richards, 1992; Sear, 1996; Haynes and Pender, 2007), short distance movement during partial transport (Sear 1996), and the formation of structural elements (e.g. pebble clusters, ribs, polygons) during transport (Oldmeadow and Church, 2006).

Biological activity can also alter the structure of surface gravels (Johnson *et al.*, 2010). Hydraulic, sedimentological and bed structure contrasts are to be found across a wide range of scales in gravel-bed rivers, from the presence on the bed surface of individual patches of contrasting grainsize (Vericat *et al.*, 2008); through step-pool and riffle-pools (Milne, 1982; Clifford, 1993; Sear, 1996) to large bar scale facies contrasts (Rice and Church, 2010). Hence, there are spatial controls on entrainment via structural contrasts that will influence bed mobility and the evolution of bed morphology.

Riffle-pool sequences are a near-ubiquitous bed morphology of alluvial gravel-bed rivers. They are characterised by strong hydraulic contrasts at long duration, low magnitude flows, and a progressive equalisation or even reversal in the strength of these contrasts at higher in-bank flows (Keller, 1971; Booker *et al.* 2001; Milan *et al.*, 2001). Whilst considerable research has focussed on the hydraulic mechanisms by which riffle-pool sequences are maintained, relatively few studies have examined the sedimentological and structural controls on sediment transport. This dearth of studies pertains despite published evidence for distinct sedimentological contrasts between individual units of the riffle-pool sequence (Lisle, 1989; Milne, 1982; Clifford, 1993; Sear, 1996). Sear (1992; 1996) and Clifford (1993) independently developed a hypothesis that linked near bed turbulence to the evolution of tightly packed and structured surface sediments on riffles that resulted in higher critical shear stress for particles on riffles compared with pool subunits. They hypothesized that these differences were sufficient to maintain riffle-pool morphology. However, this differential sediment entrainment hypothesis (DSEH) remains untested, meaning that the relative roles of velocity reversal and sedimentological contrasts in maintaining riffle-pool topography are unknown.

We present the first quantitative test of the DSEH by using new technology to quantify grain-scale properties relating to grain entrainment and sediment fabric in different sub-units of the riffle-pool sequence. Terrestrial Laser Scanning (TLS) enables the collection of *in-situ* high-resolution information on exposed bed micro-topography (Hodge *et al.*, 2009a, 2009b; Heritage and Milan 2009), providing measures of surface grain size, packing and fabric, including: distribution of surface elevations (distribution of surface elevation relative to grainsize provides information on packing and surface rugosity/ roughness); semivariograms; grain exposure (Schmeekle and Nelson, 2003; Kean and Smith, 2006) and particle alignment (Smart *et al.*, 2004). In this paper we 1) use TLS data and other field measurements to identify spatial variations in sediment structure through a riffle-pool sequence; 2) use the field data to parameterise a modified form of the physically-based entrainment model of Kirchner *et al.* (1990) in order to predict spatial variation in critical entrainment shear stress; and 3) compare the predicted critical entrainment shear stresses with the spatial distribution of shear stress predicted by a 2D CFD model in order to assess the relative roles of sediment structure and hydraulics in causing any preferential sediment entrainment.

2. Methods

In the methods we first outline the physically-based entrainment model that is parameterised using the field data. We then present the field site and the suite of field measurements that were collected. Finally, the CFD model set-up is described.

2.1. Grain entrainment model

In order to quantify spatial variations in critical entrainment shear stress (τ_c) between riffles, pool and pool exits, we use a modified form of a physically-based model of grain entrainment (Kirchner *et al.*, 1990). The key parameters in this model, grain size, exposure, pivoting angle and resistance to lift forces, are parameterised from the field measurements (see following sections).

At the threshold of motion the following force balance applies to a grain:

$$\frac{F_D}{\tan\Phi} + F_L = mF_W = m\frac{1}{6}(\rho_s - \rho)g\pi D^3 \qquad (1)$$

where F_D and F_L are respectively the drag force and the lift force, F_W is the immersed weight of the grain, m is a multiplier of F_W that incorporates the effect of additional resistance to grain entrainment (e.g. grains being held in place by a cohesive mortar), Φ is the grain pivoting angle, ρ_s is the density of sediment (taken as 2650 kg m^{-3}), ρ is the density of water, g is the acceleration due to gravity and D is the grain diameter. The incorporation of m in equation 1 is an amendment to the equations of Kirchner *et al.* (1990). The model of Kirchner *et al.* (1990) calculates the shear stress that solves equation 1 through consideration of grain geometry and an assumed logarithmic flow velocity profile.

To calculate values for F_D and F_L, a relationship between flow velocity and height above the bed is also needed:

$$u(z) = \sqrt{\tau/\rho}\,\frac{1}{\kappa}\ln\left(\frac{z+z_0}{z_0}\right) \qquad (2)$$

where $u(z)$ is the flow velocity at height above the bed z, τ is the boundary shear stress, κ is von Kárman's constant (taken as 0.4) and z_0 is the roughness height (assumed to be $0.1D_{84}$; Whiting and Dietrich 1990). The reference height $z = 0$ is assumed to be the local mean bed elevation. Equation 2 is only applicable when $z > 0$, otherwise $u(z) = 0$. F_D is calculated as:

$$F_D = \frac{C_D}{2} \rho \int_{p-e}^{p} W(z)\, u(z)^2\, dz \qquad (3)$$

where $W(z)$ is the width of the grain cross-section at height z, C_D is an empirical drag co-efficient assumed to be 0.4 (Wiberg and Smith, 1985), p and e are respectively grain protrusion and exposure. F_L is calculated as:

$$F_L = \frac{C_L}{2} \rho A \left[u(p)^2 - u(p-D)^2 \right] \qquad (4)$$

where A is the plan view cross-sectional area of the grain and C_L is an empirical lift coefficient assumed to be 0.2 (Wiberg and Smith, 1985). The boundary shear stress at the threshold of motion, τ_c, is calculated by rearranging the preceding equations (for the full derivation see Kirchner *et al.*, 1990):

$$\tau_c = 0.1 (\rho_s - \rho)\, g \left(\frac{\pi D^3}{6}\right) \left\{ \frac{C_D}{2\kappa^2} \int_{p-e}^{p} \sqrt{D^2 - \left[2(z-p) + D\right]^2}\, f(z)^2\, dz + \frac{C_L \pi D^2}{8\kappa^2} \left[f(p)^2 - f(p-D)^2 \right] \right\}^{-1} \qquad (5)$$

where:

$$\begin{aligned} f(z) &= \ln\left(\frac{z + z_0}{z_0}\right) && z > 0 \\ f(z) &= 0 && z \le 0 \end{aligned} \qquad (6)$$

Kirchner *et al.*'s [1990] equation is multiplied by 0.1 so that inputs in S.I. units produce a value of τ_c in Pa. Equation 5 assumes that grains have a circular cross-section. A dimensionless value of τ_c, (τ_c*) is calculated as:

$$\tau_c^* = \frac{\tau_c}{(\rho_s - \rho) g D} \qquad (7).$$

2.2. Field site and field methods

Field data were collected from Bury Green Brook, Hertfordshire (51° 50' N, 0° 4' E), a small stream with a well-defined riffle-pool morphology (Figure 1). The study reach varies in bankfull channel width from 2.8 to 6.5 m. The mean bed slope over the ~80 m reach is 0.008 and the mean flow depth (variable over pools and riffles) at bankfull discharge is 1.3 m. Bury Green Brook drains a rural catchment of 21.8 km^2, underlain by Upper Chalk which is extensively overlain by boulder clay and glacial sands, with gravel and alluvium in the valley floor. This combination results in a flashy hydrograph and sustained flows over the autumn-spring flood season, with a dry bed during the summer months. These conditions create bed mobilising events in most years, followed by periods when the dry water-worked river bed can be accessed enabling Terrestrial Laser Scanning and other field data to be collected. No flow gauging exists for the stream hence flow data are unavailable for the site. Data including TLS were collected from ~ 1 m^2 patches of the river bed in both September 2006 and June/July 2009. For the flow modelling, an 80 m reach was surveyed using TLS in 2009. The reach included five pool-riffle sequences.

2.3. Patch-scale field data

Patch scale data were collected in both years. These data provide values of D, Φ, m, p and e for grains in the different facies, which are used to parameterise the modified model of Kirchner *et al.* (1990). The data also provide supplementary evidence on sediment structure. Representative patches were selected from the different facies present in the channel: pools, riffles, pool exits and pool heads. These facies were visually identified and the local flow direction was estimated from the channel topography and the alignment of wake deposits (sensu Reid *et al.*, 1992). Subsequent analysis of the channel long-profile and hydraulics confirmed the field identification.

The analysed patches comprised two pools, two pool exits and two riffles in 2006 and four pools, three pool exits, three riffles and one pool head in 2009. Analysis primarily focuses on the 2009 patches. From each patch, the following measurements were taken: 1) Terrestrial Laser Scanner (TLS) data to record the grain-scale patch topography; 2) pivoting angle measurements from individual grains, 3) lift force measurements from individual grains; 4) bulk grain size distribution.

TLS data

TLS data were collected from each patch following the method of Hodge *et al.* (2009a). Data were collected from two opposing scanner positions, at a point spacing of 2 mm (for comparison, the finest median grain size is 18 mm). Three repeat scans were collected from each scanner position. The multiple scans were averaged and filtered following Hodge *et al.* (2009a), and Digital Terrain Models (DTM) were interpolated from the point data at 1 mm spacing. DTMs were detrended in order to remove the influence of reach-scale topography; detrending was achieved by fitting a second order polynomial surface to the DTM, and then subtracting this surface from the DTM. The mean patch elevation was subtracted from the DTM to produce a mean elevation of 0 m. The patch bed slope (β) was determined by initially calculating the slope between all pairs of elevations 10 cm apart in the downstream direction, and then taking the mean of all these slopes. Analysis of the DTMs can also provide information on sediment structure. Given the relatively small size of the grains compared with the resolution of TLS data, such analysis is here limited to distributions of surface elevations (Hodge *et al.*, 2009b) and the exposure of individual grains.

Pivoting angle measurements

Pivoting angles are a function of the horizontal force required to entrain a grain and therefore are a measure of grain geometry and packing. Following Johnston *et al.*, (1998) pivoting angle (Φ) is estimated using:

$$\tan(\Phi) = \frac{F_d - F_W \sin(\beta)}{F_W \cos(\beta)} \tag{8}$$

where F_d is the maximum horizontal force required to dislodge the grain. Force was applied using the probe of a force gauge, with the gauge recording the maximum force. F_W is the weight of the grain and the bed slope, β, is positive if bed elevation increases downstream. Accounting for the effect of β is important when $|\beta|$ is > 2° and Φ is < 70°. In 2006, pivoting angles were measured for 39 or 40 grains per patch, and in 2009 for 50 grains per patch.

Lift force measurements

For unconstrained grains, the lift force (F_L) required to vertically entrain a grain is equal to the grain weight (F_W). To quantify the extra force required to overcome any additional impediments to grain entrainment, such as grain packing and mortaring, F_L is expressed as a multiple of F_W, which is termed m: $m = F_L/F_W$. Lift forces were measured for between 14 and 25 grains in each of the 2009 patches (with the exception of patch P4). Grains were selected using a grid. A 20 cm length of nylon string was stuck to the middle of the exposed area of each grain using a bead of superglue without disturbing the grain. A force gauge was then used to measure the maximum force required to vertically entrain the grain. For each grain, grain weight and axes dimensions were also recorded.

Bulk grain size distribution

Samples for bulk grain size analysis were collected from the 2009 and 2006 patches by skimming the surface layer from an undisturbed area of the patch. The sediment samples were dry sieved through half-phi sieves and weighed.

Grain exposure

Grain exposure was measured for individual grains in the DTMs. Grains were selected using a grid, and manually digitised with cross-reference to photographs of the patches. Only grains with a long axis of > 20 mm were digitised; smaller grains were harder to identify unambiguously. If no grain could be identified at the grid intersection, then a nearby grain was digitised. Between 20 and 45 grains were digitised from each 2009 patch, with the exception of patch E3 where the DTM quality was too poor. In the Kirchner *et al.* (1990) model, grain exposure is represented through 1D measures: grain exposure (e) and grain projection (p, Figure 2c). Two further measures that better take into account the 2.5D nature of the TLS data are also included for comparison; these are profiles of exposed width of the grain (which describes direct sheltering) and of the extent of sheltering from upstream grains (Figure 2).

Grain projection, p, is the difference between the maximum height of the grain and the local mean bed elevation (Kirchner *et al.*, 1990). The local bed is the area of the bed that extends a distance equal to D_{84} upstream and downstream of the grain. D_{84} is calculated from the GSD measured from the grains used in pivoting angle and lift analysis. e is defined as the difference between the maximum height of the grain and the maximum upstream elevation; maximum upstream elevation is measured in the area that extends a distance equal to D_{84} upstream of the grain. If the maximum upstream elevation and the maximum grain height occur at different positions across the face of the grain, then this definition underestimates grain exposure. To incorporate the cross-stream profile of the grain, e was calculated for mm-wide, flow-parallel strips across the cross stream profile, with the maximum grain height and elevation being those measured within that strip. If the grain elevation was less than the maximum elevation, $e = 0$. The value of e for the grain is the mean of e for all strips.

Grain exposure is produced by two components: direct and remote sheltering (McEwan *et al.*, 2004). Direct sheltering is the effect of contacting upstream grains reducing the effective area of the grain in question. Remote sheltering is caused by the wake of upstream grains reducing the fluid drag force that is applied to the grain (Schmeeckle and Nelson, 2003; Heald *et al.*, 2004). Fluid drag is most reduced immediately behind an obstacle, with an approximately linear return to unobstructed flow over a maximum sheltering distance of eight to ten grain diameters (Schmeeckle and Nelson, 2003; Heald *et al.*, 2004). p and e are calculated over a single grain length, therefore primarily reflect direct sheltering.

To produce profiles that demonstrate the effects of both direct and remote sheltering over the elevation of a grain, the exposed face of each digitised grain is divided into cells 1 mm wide by 0.2 mm high. At each elevation, the width of the exposed face (W, in mm) is equal to the number of cells. Plotting W against height (h) (Figure 2d) profiles the shape and height of the exposed grain face and hence the area of the grain that is not affected by direct sheltering. For comparison between grains, W and h are normalised by grain diameter D.

To quantify the effect of remote sheltering, a weighting (s) is calculated for each cell as:

$$\begin{aligned} s &= d_u / d_t \qquad & d_u &\leq d_t \\ s &= 1 & d_u &> d_t \end{aligned} \tag{9}$$

where d_u is the distance of the first upstream grain sheltering that cell, and d_t is the maximum sheltering distance; d_t is taken to be 200 mm, which is broadly consistent with sheltering occurring over eight to ten grain diameters. Figures 2a and b show an example of the distribution of s over the exposed face of a grain. s is inversely proportional to the reduction in flow strength and hence the degree of remote sheltering. Profiles of mean s against h/D show the vertical variation in s (Figure 2e), indicating how remote sheltering varies down the grain face.

2.4. 2D flow modelling

The field data and grain entrainment model will demonstrate the effect of sediment structure on τ_c in different facies. However, whether or not a grain is entrained also depends on the magnitude of the bed shear stress (τ) applied to that grain. Shear stress in riffle-pool sequences is spatially variable (Booker *et al*. 2001; McWilliams *et al.*, 2006), and therefore it is instructive to compare the magnitude of spatial variation in applied τ with the magnitude of variation in τ_c. We do not have flow data from the ungauged Bury Green Brook, and so cannot directly calculate τ. Instead we use a 2D flow model to reconstruct a bankfull event and to estimate the magnitude and spatial distribution of τ.

Flow processes in riffle-pool sequences are strongly 2D and potentially 3D (Booker *et al*. 2001; McWilliams *et al.*, 2006). Although this may suggest the use of a 3D flow model, 3D flow models require spatially distributed 3D velocity data for calibration and verification (Lane *et al.*, 1999), which are not available for this ephemeral river. Use of a 2D model provides a balance between model capability and complexity (Cao *et al.*, 2003), and so we estimate τ using the depth-averaged 2D flow model Hydro2de (Beffa and Connell, 2001). Hydro2de solves the Navier-Stokes depth-averaged shallow water flow equations in conservation form, in which depth and specific flow are related to spatial coordinates [x, y] using conservation of volume and momentum. Bed shear stresses are calculated using the Manning's friction law (Beffa and Connell, 2001). Hydro2de can reproduce spatial variations in bed topography and roughness, which are a key feature of riffle-pool sequences. Using a 2D model to calculate bed τ in a riffle-pool sequences is supported by the work of Pasternack *et al.* (2006) and Cao *et al.* (2003).

Our validation data is limited to a series of trash line elevations that correspond to a bankfull event. These trash lines were mapped with a total station, and provide an estimate of water depth and water surface slope. As our flow modelling is therefore relatively poorly constrained, we identify the effect that both discharge and roughness parameterisation have on the distribution of τ, and propagate this analysis through to the comparison with the entrainment model results. We also consider the extent to which our conclusions are sensitive to the exact values of the flow model results.

To construct a reach scale DEM for input to Hydro2de, TLS was used to measure the topography of the channel and banks at a mean point spacing of 0.01 m. The TLS data were subsequently processed through a combination of manual point cloud editing and automated minimum elevation filtering to remove extraneous data. The latter process involves gridding the data at a coarser resolution of 0.1 m, and then retaining the minimum elevation within each cell, thereby increasing the likelihood that the chosen point is representative of the bare earth model. The output DEM, with a grid spacing of 0.1 m, was used for the flow modelling.

Hydro2de can operate using spatial distributions of roughness, defined in the model using dimensionless Manning's n values. Manning's n was calculated using the formula devised by Ferguson (2007):

$$(8/f)^{1/2} = a_1 a_2 (R/D_{84}) \Big/ \left[a_1 + a_2 (R/D_{84})^{5/3}\right]^{1/2}, \quad n = R^{1/6}(f/8g)^{1/2}, \qquad (10)$$

where *f* is the Darcy-Weisbach friction factor and *R* is the hydraulic radius, and with a_1 = 6.5 and a_2 = 2.5 as suggested by Ferguson (2007; 2010). Ferguson (2007)'s formula is an improvement over the commonly used Strickler formulation because the former accounts for the effect of relative submergence on Manning's n. We note however that under bankfull conditions in Bury Green Brook, R/D_{84} varies between ~ 7 (riffles) and ~ 14 (pools), and thus values of Manning's n calculated using equation 10 and the Strickler formulation are not greatly different.

Values of Manning's n were calculated for all patches with grain size data. *R* was calculated for each patch under the flow conditions described by the trash marks. The trash data were interpolated to produce a best fit water surface for this flow event, and the elevation of this surface was used to calculate *R* at each patch location. Hydro2de was parameterised using an average value of Manning's n from the riffle patches for all riffle areas (n = 0.034), whereas individual values of Manning's n were used for the pools (n = 0.03 to 0.031). This is because the pools were spatially isolated, whereas it was not always possible to identify clear boundaries between the different riffles. The roughness of the banks was set at n = 0.1 according to values derived from a stream with comparable bed and bank morphology and roughness (Booker *et al.*, 2001).

The flow model was run at seven different discharges between 2.2 and 2.8 m^3s^{-1}; the discharge that best replicated the bankfull conditions was identified by calculating the RMSE between the modelled water surface and the water surface interpolated from the trashlines. This range of discharges is comparable to bankfull flows recorded for an adjacent similar sized stream (Stansted Brook; gauge number 38028, drainage area: 25.9 km^2).

Identifying an appropriate value of Manning's n is a known source of uncertainty in flow models, and we note that we are applying a relationship derived from 1D data to a 2D model. We therefore also used a high and a low parameterisation of Manning's n to quantify the effect on τ. Ferguson (2010) compiled measured values of Manning's n from > 400 rivers. We used the spread of these data (in Figure 2B in Ferguson, 2010) to identify plausible upper and lower values of Manning's n at values of R/D_{84} that are relevant to the riffles and pools in Bury Green Brook. The low Manning's n parameterisation is n = 0.017 and n = 0.014 for riffles and pools respectively, and the high parameterisation is n = 0.097 and n = 0.051. Both parameterisations were run at the same range of discharges as the standard parameterisation. For the higher

Manning's n parameterisation these discharges flooded the model domain, and so a range of lower discharges between 1.4 and 1.8 m^3s^{-1} were also run.

3. Field results

Results are presented from the grain-scale field measurements and CFD modelling. The field data are then used to parameterise the grain entrainment model. This section analyses the grain-scale properties to identify how they vary both within and between facies, and whether they vary as a function of grain size.

3.1. Grain size data

Grain size distributions (Figure 3) were calculated from both a bulk surface sample (2009 patches) and the grid-based samples of grains used for the pivoting and lift analyses (2006 and 2009 patches). The former describes the GSD by weight of the entire armour layer, whereas the latter gives the GSD by area of the surface grains, and therefore is more representative in terms of the grains that will contribute to bedload transport. GSD percentiles used in subsequent analyses are calculated from the grid-based samples.

Although most patches have similar GSDs, riffle patches tend to be coarser, whereas pool and pool exit patches tend to be finer. For the 2009 grid-based GSDs, pool patches have D_{50} between 27 and 38 mm, pool-exit patches have D_{50} between 28 and 37 mm and riffle patches have D_{50} between 35 and 42 mm. This pattern of finer pools and pool-exits and coarser riffles is also found in the 2006 data. 2006 patches tend to be finer than 2009 patches of the same facies; 2006 pools have D_{50} between 18 and 26 mm, 2006 pool exits have D_{50} between 18 and 30mm and 2006 riffles have D_{50} between 24 and 33 mm. Grain sphericity does not vary significantly between the different facies (ANOVA, $p = 0.31$), with a mean value of ~ 0.7. Grain form (a-b/a-c, where a, b and c are axes lengths) does vary significantly between the facies (ANOVA, $p = 0.002$); however, the difference in mean value between facies is small (mean form values for pool, pool exit and riffle facies are 0.56, 0.55 and 0.48).

3.2. Pivoting angles

Distributions of pivoting angles (Φ) from both 2006 and 2009 (Figure 4a and b) show that pools tend to have lower values and a larger range of Φ, whereas pool exits tend to have higher values of Φ and a narrower range. Riffles typically fall somewhere between these two extremes. The main difference between the 2006 and 2009 data is that the 2006 values of Φ for a given facies are generally higher than those from 2009.

For both the 2006 and the 2009 data, analysis of covariance of Φ as a function of both facies and relative grain size (D/D_{50}) indicates that both facies and D/D_{50} have a significant influence on pivoting angle (respective p-values of < 0.0001 and < 0.0001 for 2006 and < 0.0001 and 0.02 for 2009). Differences between facies are further identified by fitting linear regressions to Φ as a function of D/D_{50} for all data from each of the facies. For the 2009 data, this analysis reveals a significant difference between the regression slopes of the pool and pool exit facies (significant at $\alpha = 0.05$) but no significant difference in regression intercepts. Regression lines fitted to the different 2006 facies are not significantly different. Using the same analysis to investigate similarities between patches within a facies from the same year reveals no significant difference in regression slopes, and a significant difference in intercepts only between 2009 patches E1 and E3. This indicates that there is greater variability between facies than within patches from a particular facies.

Values of Φ display a large amount of scatter for a given value of D/D_{50}, as has been identified in previous investigations (Kirchner *et al.*, 1990; Johnston *et al.*, 1998). Percentiles of Φ calculated for binned values of D/D_{50} (Figure 4) show that in the 2009 pool facies, percentiles of Φ are approximately evenly distributed for a given value of D/D_{50}, whereas in the 2009 riffle and pool exit facies, the upper 60 % of the values of Φ fall between 80 and 90°. The 2006 data show a similar pattern, but with higher values of Φ.

Pivoting angles have previously been measured for *in-situ* grains in the field by Johnston *et al.* (1998). Values of Φ measured in Bury Green Brook are generally higher than those measured by Johnston *et al.* (1998); fits of the form:

$$\Phi = a(D_i/D_{50})^{-b} \tag{11}$$

to the Bury Green Brook data predict that a grain of size D/D_{50} = 1 will have a mean Φ of 62° in the pool facies, 83° in the pool exits and 76° in the riffles. In contrast, for the same relative sized grain, Johnston *et al.* (1998) predict mean Φ of between 49 and 62°. The field sites of Johnston *et al.* (1998) have similar D_{50} to the Bury Green Brook patches. The difference between the two sets of results could be because Johnston *et al.* (1998) selected field patches that lacked spatial sorting and clustering and had little sand or silt among the gravel, thereby choosing patches more similar to the Bury Green Brook pools. An alternative explanation could be sampling strategy; Johnston *et al.* (1998) randomly sampled available particles (i.e. those that could move without first moving other grains), whereas the grid-based sampling applied in Bury Green Brook meant that pivoting angles were measured regardless of grain availability.

3.3. Lift forces

Lift force measurements (*m*) also vary between the facies (Figure 5). Generally, grains in pools have lower values of *m* (mean *m* for all pool measurements is 1.5), whereas grains in pool exits have higher values (mean *m* for all pool exit measurements is 2.7). Lift forces are not a significant function of relative grain size (Figure 5); linear regression of *m* against D/D_{50} for all data from a given facies does not show a significant relationship for either the pool or riffle facies (at $\alpha = 0.05$). For the pool exit facies, $p = 0.01$; removing the outlying point at $D/D_{50} = 2.4$ increases p to 0.02. Mean values of *m* are not significantly different between patches from the same facies (ANOVA, $p > 0.09$). Mean values of *m* are, however, significantly different between the different facies (ANOVA, $p < 0.0001$). Furthermore, the mean value of *m* in the pool exit patches is significantly greater than in the other three facies.

In the field, the high values of *m* for grains in the pool exit patches were identified as being the result of mortaring, i.e. the presence of a layer of cohesive fine-grained sediment that cements grains together. Of the lift measurements, mortaring was identified as affecting 53 % of the pool exit grains, 18 % of the riffle grains and 17 % of the pool grains. Furthermore, the pool exit grains with mortaring had a mean *m* value of 3.9, whereas for grains without mortaring, mean *m* was 1.4. The presence of mortaring is not apparent in the bulk GSDs though; although patch E2 has a high proportion of fine sediment, neither patch E1 nor E3 has elevated levels of fine sediment (Figure 3a).

3.4. Grain exposure

Grain protrusion and exposure

Grain protrusion (p) and exposure (e) provide a 1D measure of grain exposure (Figure 2). Both p and e are normalised by D. p/D shows no significant relationship with D/D_{50} (Figure 6a); regression lines all have a p-value of at least 0.08 and the slopes are not significantly different to zero. Distributions of p/D are significantly different between facies (ANOVA, p = 0.0001), with the mean value of p/D for grains from pool patches being significantly higher than the mean for grains from either pool exit or riffle patches.

Distributions of p/D for all grains from a facies are not significantly different to a normal distribution; depending on the facies the mean varies between 0.37 and 0.47 and the standard deviation between 0.16 and 0.21. Grain exposure (e/D) shows a strong linear relationship with p/D (Figure 6b); linear regressions of e/D against p/D for each facies having a regression p-value of < 0.0001. Residuals from this relationship are described by a normal distribution.

Direct and remote sheltering

Grain exposure is a function of both the area of the grain projecting above the boundary between the grain and upstream neighbouring grains, and the extent of sheltering applied by upstream grains (Figure 2). Both components vary with elevation from the top to the bottom of the grain. Figure 7a shows how the median width of the exposed grain area (W) varies with height below the top of the grain (h). Both h and W are normalised by D, and W/D for a completely exposed sphere is added for comparison. Data from each facies displayed considerable variation between the profiles of individual grains because of the variable grain shapes and geometry of sheltering grains. Consequently, the 95 % error bands around the median value of W/D are relatively wide. Within each facies, there was no systematic difference between profiles of W/D for different sized grains, down to the size of the smallest identified grains (20 mm).

For all facies, in the upper part of the profile from $h/D = 1$ to h/D between 0.8 and 0.9, median W/D is approximated by the profile of a sphere. Below this, W/D is less than the value of W/D for a fully exposed sphere. By $h/D = 0.5$, all profiles of median W/D drop to $W/D < 0.2$. This result is consistent with grains being embedded in the surface by about half their diameter. Between $h/D = 0.5$ and 0.8, the grains in pool patches have the highest median value of W/D. Pool exit grains display the smallest values. This difference between pool and pool exit grains can be attributed to differences in grain packing between the different facies. An alternative explanation of differences in grain shape can be ruled out because there is no significant difference between the different facies in the ratio of the $a:b$ axes of the grains for which exposure was calculated (ANOVA, $p = 0.34$).

Profiles of the median sheltering weighting (s), i.e. the median distance of upstream sheltering grains, also show a difference between the facies (Figure 7b). In each facies, as h/D decreases, s decreases, i.e. grains become more sheltered. For any given value of h/D, the profile from pool grains has the highest value of s, indicating the least sheltering, whereas riffle grains are the most sheltered; this variation indicates a difference in sediment packing between these facies.

3.5. Surface elevations

Grain exposure measurements indicate that grains in pool patches are relatively more exposed than grains in other facies, suggesting a difference in grain packing. This difference can also be seen in the distributions of surface elevations in the DTMs (Figure 8). The DTMs have been detrended, therefore the distribution of elevations reflects the geometry of the patch at the grain-scale. A large range of elevations suggests that grains are loosely packed, whereas a narrower range indicates tighter packing. When elevations are normalised by D_{50}, pool patches generally have a higher range of elevations that other patches, with the range between the 5th and 95th elevation percentiles being between 0.99 and 2.01D_{50}. Riffles consistently have a narrower range of elevations, with the range from the 5th to the 95th percentiles being from 0.73 to 1.10 D_{50}. The 2009 pool exit patches also have a narrow range of elevations, whereas the 2006 pool exit patches have a much larger range.

3.6. Field results summary

Field measurements and analysis of DTMs from different facies within Bury Green Brook have identified significant differences between the facies in terms of the grain-scale properties. These differences in turn will influence the critical shear stress at which grains from the difference facies are entrained. Furthermore, the data also help to identify the aspects of sediment geometry that are causing these differences.

The field data show that grains in the pool patches, in comparison with the other patches, have relatively lower pivoting angles and relatively higher grain exposure, both in terms of total exposed area and the location of upstream sheltering grains. Lift force measurements are typically only one or two multiples of grain weight, and grain sizes are relatively smaller. All of these variables suggest that grains in pool patches are likely to be more easily entrained than grains in either riffle or pool exit patches. Riffle and pool exit patches have similar grain-scale properties to each other, with the exception that grains in pool exit patches recorded higher lift forces. Grains in the pool head patch appear to have properties intermediate to the other facies, but this is limited by the single patch sample size.

The field data also suggest a possible cause of the differences in properties relating to grain entrainment. The higher grain exposure and surface roughness in the pool patches indicates that the grains are more loosely packed. Looser packing means that grains sit in shallower pockets, resulting in the lower pivoting angles. Lower exposure and roughness in the pool exit and riffle patches suggest tighter sediment packing.

The field data also describe differences between the patches in 2006 and in 2009. The relative variation in D_{50} between different facies is the same in both years, i.e. pool patches are relatively finer and riffle patches are relatively coarser. However, within a facies the 2006 patches are consistently finer than the 2009 patches. The same is also true of pivoting angle measurements. In both years pivoting angles are lowest in the pool patches; however pivoting angles measured from the 2006 patches are higher than those measured in 2009. The reasons for these temporal variations are unknown; differences in measurement technique are unlikely because pivoting angles were measured by the same person on both occasions. A plausible explanation is the magnitude and history of recent flood events. After a large transport event grains may be deposited with a range of pivoting angles, whereas subsequent smaller events may preferentially reposition grains with lower pivoting angles, increasing the average pivoting angle. Changes in sediment GSD could be a function of the connectivity to upstream sediment supplies (Hooke, 2003). The finer GSD in 2006 could also be associated with a higher degree of mortaring, which would also increase pivoting angles.

4. Flow modelling results

The flow modelling results show that the water surface elevation interpolated from the trash data can be reproduced with both the low and the standard parameterisations of Manning's n (Figure 9). There are still discrepancies at around 20 m and 38 m downstream, although these trash markers could potentially relate to a different high flow event. Note that at high parameterisations of n, the range of discharges (2.2 – 2.8 m^3s^{-1}) used for the aforementioned scenarios all flooded the model domain resulting in very high water surfaces relative to the trash markers. A range of lower discharges (1.4 – 1.8 m^3s^{-1}) were also modelled in an attempt to replicate the water surface slope as per the low and standard parameterisations of Manning's n. The lowest RMSEs are given by a discharge of 2.6 m^3s^{-1} (low n, RMSE = 0.024) and of 2.5 m^3s^{-1} (standard n, RMSE = 0.027). At high n, the lowest RMSE is given by a discharge of 1.5 m^3s^{-1} (RMSE = 0.051). This RMSE is almost twice that given by the other two parameterisations, and therefore the high n model results are not further considered.

All model runs show strong spatial variation in the distribution of both depth-averaged flow velocity and bed shear stress (τ) within the channel, with highest values typically occurring over riffles (Figure 10). For each sequence of pool, pool exit and riffle patches, τ is lowest in the pool exit, followed by the pool, with highest τ in the riffle (Figure 11). Under the optimum (lowest RMSE) standard Manning's n parameterisation, median τ in the riffle patches was between 11 and 22 Pa, whereas median τ in the pool patches was between 4 and 17 Pa. Across all seven different discharges the total range of median τ is between 4 and 18 Pa in pools, and 10 and 23 Pa in riffles. Values of τ are lower under the optimum low Manning's n parameterisation, with median riffle τ between 2 and 6 Pa, and median pool τ between 1 and 4 Pa; these ranges are the same as the total range across all seven discharges. These results indicate that, under bankfull conditions, maintenance of the pool-riffle sequences in the study reach appears not to be the result of a velocity or shear stress reversal.

The validity of the modelled shear stress estimates is difficult to assess further due to the lack of suitable validation flow data. Furthermore, an alternative method for calculating shear stress, the reach averaged depth-slope product, is not comparable because of its assumption of uniform flow (flow through riffle-pool sequences is typically non-uniform, Figure 2) and the fact that it tends to overestimate the effective shear acting on a grain (Robert, 1990). Taking these uncertainties into account, we carry forward both the low and standard Manning's n parameterisations to a comparison with the entrainment model results.

5. Grain entrainment model

5.1. Model results

The field data are used to derive the parameters for the grain entrainment model of Kirchner *et al.* (1990). Using a Monte-Carlo approach and equation 5, values of critical entrainment shear stress (τ_c) are calculated for a large number (4800) of simulated grains from each of the pool, pool exit and riffle facies. The properties of each of these grains are determined as outlined in Table 1. Pivoting angle is calculated as a function of relative grain size, whereas other properties were not found to be size dependent. Grain exposure is parameterised using *p* and *e*, which only includes the sheltering effects of grains up to a distance of D_{84} upstream. In order to calculate exposed grain area, grains are assumed to be spherical. This assumption does not greatly affect the calculations. In terms of F_W, the ratios of a/b and c/b for an average grain are such that $a/b \times c/b \approx 1$, therefore the volume of a grain is well approximated by the volume of a sphere with diameter b. In terms of F_D, the potential exposed grain area is assumed to be a circle with diameter b. Use of an ellipse with width b and height c only increases predicted widths by up to 20 %. Such discrepancy is small compared to the differences between idealised and actual exposure profiles shown in Figure 7.

In the field, different parameter values were measured from different grains, therefore possible relationships between parameters (e.g. pivoting angle and exposure) cannot be quantified from the field data. Such parameter values, however, are not likely to be completely independent of one another, as shown in the theoretical relationships derived by Kirchner *et al.* (1990). For example, a grain in a shallow pocket in the bed will have both a low pivoting angle and a high exposure. Furthermore, values of Φ and m measured in the field are likely to be related, as they will both capture the effect of properties such as mortaring; for example patches E1 and E2 have high values of both variables.

In order to investigate the effect of these possible inter-relations, the grain entrainment model is run in two forms, A and B. In model A, Φ and p for a single grain are assumed to be independent of each other, and field measurements of Φ are assumed to incorporate the effect of mortaring and therefore the value of m for all grains is 1. In model B, for each grain, Φ is inversely proportional to p. If the percentile randomly selected to interpolate a value of Φ is *n*, then the selected value of *p* is that of the 100 – n^{th} percentile of the relevant normal distribution. The effect of mortaring on lift forces is incorporated by selecting values of *m* from the field data distributions. Model A is more strictly derived from the field data, and, by setting $m = 1$, does not allow the effect of mortaring to be potentially double counted; it therefore is a more conservative model. Model B is more speculative; the proposed relationship between Φ and *p* is consistent with Kirchner *et al.* (1990), but cannot be tested with the field data. Furthermore, both Φ and *m* may include the effect of mortar. Model B estimates the additional influence of these factors.

Distributions of τ_c calculated for the three different facies and from the two model variants are shown in Figure 12a. Using model A, grains in the pool facies have the lowest values of τ_c, with a median of 37.7 Pa. Grains in pool exit and riffle facies have increasing values of τ_c, with respective medians of 52.6 and 65.4 Pa. The mean values of τ_c from the different facies are significantly different to each other (ANOVA of $\log(\tau_c)$, $p < 0.0001$).

Using model B, grains from the pool again have the lowest values of τ_c. The median value of τ_c of 36.2 Pa is similar to that in model A, but 17 %, rather than the previous 7 %, of grains have values of $\tau_c < 20$ Pa. Model B produces distributions of τ_c for pool exit and riffle grains that are more similar to each other, although the median values of τ_c are reversed; median τ_c is 77.4 Pa and 68.1 Pa for the pool exit and riffle grains respectively. This similarity between the two distributions is mainly because of an increase in the value of τ_c for pool exit grains. Both distributions have a longer tail of lower values in model B than in model A. Mean values of log(τ_c) for all three facies are again significantly different from each other.

The longer low value tails in model B results are because of the inverse relationship between Φ and p; a low value of Φ is automatically coupled with a high value of p, both of which produce a lower value of τ_c. Such pairings will be less common in model A, and therefore there are fewer grains with low values of τ_c. The higher values of τ_c for pool exit grains in model B is the effect of incorporating field measurements of m, which were highest in pool exit facies.

To isolate the effects of grain size and sediment structure, models A and B were also run using the pool exit and riffle GSDs, but with pivoting angle and exposure parameterised from the pool field data. The resulting median values of τ_c were 38.5 and 47.2 Pa for the pool exit and riffle GSDs respectively for model A and 36.8 and 44.2 Pa for model B. The effect of the observed tightly packed sediment structure (expressed through p, e and Φ) in the pool exit and riffle facies is therefore to increase median τ_c by between 37 and 39 % in model A and between 54 and 110 % in model B. The larger increase in model B is because of the higher values of m.

The relationship between D/D_{50} and τ_c* (Figure 12b) predicted by the grain entrainment model shows that τ_c* is inversely proportional to D/D_{50}, with linear regressions of log (τ_c*) against log(D/D_{50}) having a gradient of ~ −1. This is consistent with the results of other studies presented by Johnston *et al.* (1998). This relationship shows that within a facies τ_c is approximately invariant with grain size, and therefore grain entrainment is also controlled by factors including sediment structure.

5.2. Comparison with flow modelling

Comparison between the distributions of τ_c predicted using the modified Kirchner *et al.* (1990) model (Figure 12) and the distributions of τ predicted from the CFD model (Figure 11) allow initial estimates of the stability of sediment in different units of the channel to be assessed. The flow modelling produced two alternative parameterisations that could not be distinguished between on the basis of the trash elevation data, and therefore we present results from both low and standard Manning's n parameterisations. For this assessment, shear stress data from different patches within the same facies are combined, and are compared with entrainment model results using both models A and B.

In each of the four different comparisons (low and standard Manning's n, entrainment models A and B), grains in pools are the most likely to be entrained (Figure 13). Under the standard Manning's n parameterisation and optimum discharge, results from models A and B respectively give an average entrainment of 1.8 % and 5.6 % in pools, with 12 % and 22 % entrainment under the highest values of τ. In contrast, entrainment in riffles reaches a maximum of 5.9 % under both models. Grains in pool exits are the most stable, with a maximum of 1.9 % entrainment. Comparisons using flow model runs with different values of discharge give very similar results (Figure 13a). Using the data from the low Manning's n parameterisation and optimum discharge produces the same pattern of results, but with lower proportions of entrainment (Figure 13b). Maximum entrainment from pools is 0.6 and 3.5 % for entrainment models A and B respectively, whereas entrainment from riffles is a maximum of 0.3 % and from pool exits is a maximum of 0.01%. Again, flow data from different discharges produces comparable results (Figure 13b).

From consideration solely of the predicted shear stress (Figure 11), sediment would be expected to be most mobile under the highest shear stresses experienced by riffles. Comparison between the flow and entrainment model results suggests that the effect of sediment structure on τ_c is such that it reverses the pattern of sediment mobility to one where under bankfull flow, sediment in pools is most mobile. In Bury Green Brook, sediment structure alone appears to be sufficient to maintain the riffle-pool topography.

This conclusion holds across both the low and standard Manning's n flow model parameterisations and across a range of discharges within each. Furthermore, the general conclusion that under high flow grains are more mobile in pools than in riffles also holds under a range of alternative flow model results. If the shear stresses over pools and riffles are both over- or underestimated, or shear stress over pools is underestimated and/or shear stress over riffles is overestimated, grains in pools will still be more likely to be entrained than riffle grains. This difference in mobility may not hold if pool shear stresses are overestimated and/or riffle shear stresses are underestimated. However, in order to equalise the probability of entrainment from pools and riffles under the standard Manning's n parameterisation, it is necessary either to reduce the predicted pool shear stresses to a third of their current values, or to increase the riffle shear stresses by 1.6. Under the low Manning's n parameterisation pool stresses need to be reduced to a fifth of current values, or riffle shear stresses need to be tripled. As such, our conclusions are valid across a range of scenarios, despite the flow modelling being relatively poorly constrained.

6. Discussion and conclusions

Whilst previous research has identified differences in the frequency of tight and loose particle structure in pool and riffle sequences (Clifford 1993; Sear 1996) and have provided some evidence for lower critical entrainment thresholds for particles in pools (Sear 1996) these have been based on rather limited datasets. The field data we report demonstrate that grain-scale sediment properties vary between different units of a riffle-pool sequence. In pools, grains have lower pivoting angles and higher exposure (Table 2), which is inferred to be a consequence of looser sediment packing. In pool exits and riffles, grains have higher pivoting angles and lower exposure as a result of closer packing (Table 2). We have used the field data to parameterise Kirchner *et al.*'s (1990) physically-based model of grain entrainment in order to predict distributions of critical entrainment shear stress (τ_c) for grains in the different facies. These model results confirm that τ_c is lowest for grains in pools; using model B, when D/D_{50} = 1, τ_c* in pools is 58% of τ_c* in riffles. Previous efforts to parameterise a similar model were speculative because of the inability to directly measure parameters such as pivoting angle and grain exposure (Sear 1996). Hence our results provide more detailed and accurate evidence for the existence of a feedback between bed fabric and entrainment thresholds. Moreover, there is a clear and repeatable spatial component to the distribution of critical entrainment thresholds.

Comparison between the flow model estimates (from different parameterisations of the flow model) and the values of τ_c predicted by the grain entrainment model suggest that sediment will be most mobile in the pools and least mobile in the pool exits. This therefore provides a mechanism by which sediment is preferentially entrained from pools, despite the fact that pools experience lower shear stresses than riffles. The findings from the field data and modelling therefore go some way towards testing the validity of the Differential Sediment Entrainment Hypothesis. Furthermore, our data support the development of differential mobility between pools and riffles, without the need for the velocity reversal that is typically assumed to be necessary for pool-riffle maintenance (Booker *et al.*, 2001; Milan *et al.*, 2001).

However, there are important differences between the field data and the conceptual model developed by Sear (1996), as outlined in Table 2. These differences principally relate to the pool-tail. In his original model, Sear (1996) postulated the pool-tail as a region of relatively fine sediment, low surface roughness and weakly developed bed structure. The result was a region of lower critical entrainment thresholds (though higher than those predicted for mid-pool regions). In this study, there are similarities to Sear's model; the low surface roughness and finer sediment, but the overall effect of these in addition to the presence of silt-clay mortar, is a higher critical shear stress than he postulated.

The presence of a layer of fine sediment at and just below the surface of the bed, has been described in studies of fine sediment infiltration (Frostick *et al.*, 1984; Lisle 1989; Sear *et al.*, 2008) and is a widely used measure of habitat impact by fisheries biologists termed "embeddedness" (Sylte and Fischenich 2002). To date the role of cohesive matrix material on critical entrainment thresholds has not been reported. In Lisle's (1989) study the matrix was largely composed of sands. Moreover previous research has tended to focus on the process of infiltration in relation to the impact on biota (Sear *et al.*, 2008) or the development of stratigraphic and sedimentological characteristics (Frostick *et al.*, 1984). In the pool exits, we show that mortaring has increased values of m (F_L/F_W) from a mean of 1.4 for grains without mortaring to 3.9 for grains with mortaring. However, the specific effect of mortaring on τ_c is difficult to quantify because it will also affect other properties such as pivoting angle and exposure. An indication of the potential effect of mortaring is given by model B. Explicit incorporation of the effect of mortaring increases the predicted median τ_c for pool exit grains by 47 % from 52.6 Pa to 77.4 Pa. Recent, independent confirmation of the importance of mortaring comes from a study of critical entrainment thresholds in ephemeral channels (Barzilai *et al.*, in review). In their study, an input of cohesive silt/clay matrix material following bank erosion resulted in a measurable increase in the shear stress required for initiation of bedload transport.

Our data have 1) demonstrated the important role of sediment structure in controlling sediment entrainment, and 2) demonstrated statistically significant spatial variability in sediment structure independent of bed material size and shape. We assume that the development of sediment structure is controlled by the time varying exposure to different hydraulic environments (Clifford 1993; Sear 1996; Haynes and Pender 2007), but we also recognise the importance of grain shape, and fine cohesive sediment. Hodge *et al.* (2009b) and Komar and Li (1986) show that elongated particles develop imbrication that results in higher bed roughness and pivot angles. In this paper, we demonstrate for the first time, the additional effect of cohesive fine sediment in mortaring framework particles. The formation of mortar in pool-tails is, we hypothesize, due to downwelling flow on the upslope of the riffle (Storey *et al.*, 2003; Tonina and Buffington, 2007) that advects suspended sediment into the surface interstices. The stability of this mortar in the presence of perennial flows is unknown. However the effect on entrainment thresholds is significant and warrants further research.

Whilst this study has focussed on the pool-riffle sequence, we hypothesize that similar magnitudes of spatial variability in critical entrainment thresholds will exist between bed fabrics in other contrasting hydraulic environments. In this work for example we did not look at the lateral variations in sediment structure in bedforms, which might be expected where pool asymmetry arises at bends. Similarly, the presence of mortaring at or downstream of local inputs of cohesive fines is widely reported in the fisheries management literature (Sylte and Fischenich 2002).

Due to the need to access the channel bed, measurements have necessarily been taken whilst the bed was exposed. Our conclusions are therefore subject to the assumption that perennial inundation will not significantly change the sediment structure; given the magnitude and repeatability of the differences between the different facies over time, significant changes are hypothesised to be unlikely, but this requires verification. Furthermore, the importance of mortaring also assumes that the matrix material is not flushed from the bed surface or infiltrated into the bed during inundation. Hence, it will be important to understand the stability of cohesive matrix materials before further conclusions can be made.

Significant research questions still remain as to the processes that result in the documented differences in sediment structure. A complete understanding will need to consider the interactions between hydraulics, sediment transport and channel morphology that drive the formation and persistence of sediment structure.

Acknowledgements

This fieldwork was funded by a research grant from the British Society for Geomorphology. Thanks to Steve Darby, Paul Carling and two anonymous reviewers for their helpful and constructive comments on earlier drafts of this paper.

Symbols

A	grain area
C_D	drag co-efficient
C_L	lift co-efficient
D	grain diameter
d_t	maximum sheltering distance
d_u	distance of upstream sheltering grain
e	grain exposure
f	Darcy-Weisbach friction factor
F_D	drag force applied to a grain
F_d	measured horizontal force necessary to dislodge a grain
F_L	lift force applied to a grain
F_W	grain weight
g	acceleration due to gravity
h	grain height
m	value of F_L/F_W necessary for vertical entrainment
p	grain projection
R	hydraulic radius
s	weighting quantifying grain sheltering
$u(z)$	velocity at height z
W	grain width
z	elevation above the bed
z_0	roughness height
β	local bedslope
κ	von Kárman's constant
ρ	density of water
ρ_s	density of sediment
τ	shear stress
τ^*_c	dimensionless critical entrainment shear stress
τ_c	critical entrainment shear stress
Φ	grain pivoting angle

References

Beffa C, Connell RJ. 2001. Two-Dimensional Flood Plain Flow. I: Model Description. Journal of Hydrologic Engineering. **6** : 397-405. DOI:10.1061/(ASCE)1084-0699(2001)6:5(397)

Booker DJ, Sear DA,Payne AJ. 2001. Modelling three-dimensional flow structures and patterns of boundary shear stress in a natural riffle-pool sequence. Earth Surface Processes and Landforms **26** : 553-576.

Barzilai R, Laronne JB, Reid I. Effect of a fine-grained matrix on bedload sediment transport in an ephemeral gravel-bed river. Earth Surface Processes and Landforms : in review.

Buffin-Belanger T, Rice S, Reid I, Lancaster J. 2006. Spatial heterogeneity of near-bed hydraulics above a patch of river gravel. Water Resources Research **42** : WO4413. DOI:10:1029/2005WR004070.

Cao Z, Carling P, Oakey R. 2003. Flow reversal over a natural pool-riffle sequence: A Computational Study. Earth Surface Processes and Landforms **28** : 689-705.

Clifford NJ. 1993. Differential bed sedimentology and the maintenance of the riffle-pool sequences. Catena **20** : 447-468.

Clifford NJ, Richards KS. 1992. The reversal hypothesis and the maintenance of riffle-pool sequences: a review and field appraisal, In Lowland Floodplain Rivers, : Geomorphological Perspectives, Carling PA, Petts GE, (eds); John Wiley & Sons, Chichester, UK; 43-70.

Ferguson, R. 2007. Flow resistance equations for gravel- and boulder-bed streams. Water Resources Research, **43**, W05427.

Ferguson R. 2010. Time to abandon the Manning equation? Earth Surface Processes and Landforms, **35**, 1873 – 1876.

Frostick LE, Lucas PM, Reid I. 1984. The infiltration of fine matrices into coarse-grained alluvial sediments and its implications for stratigraphical interpretation. Journal of the Geological Society London **141(6)** : 955-965.

Harvey JW, Bencala KE. 1993. The effect of streambed topography on surface-subsurface water exchange in mountain catchments. Water Resources Research **29(1)** : 89-98.

Haynes H, Pender G. 2007. Stress history efffects on graded bed stability. Journal of Hydraulic Engineering **133(4)** : 343-349. DOI: 10.1061/(ASCE)0733-9429(2007)133:4(343)

Heald J, McEwan I, Tait S. 2004. Sediment transport over a flat bed in a unidirectional flow: simulations and validation. Philosophical Transactions of the Royal Society of London Series A **362** : 1973-1986.

Heritage GL, Milan DJ. 2009. Terrestrial Laser Scanning of grain roughness in a gravel-bed river. Geomorphology **113** : 4-11.

Hodge R, Richards K, Brasington J. 2007. A physically-based bedload transport model for reach-scale modelling. Geomorphology **90 (3-4)** : 244 - 262.

Hodge R, Brasington J,Richards K. 2009a. *In-situ* characterisation of grain-scale fluvial morphology using Terrestrial Laser Scanning. Earth Surface Processes and Landforms **34 (7)** : 954-968.

Hodge R, Brasington J,Richards K. 2009b. Analysing laser-scanned Digital Terrain Models of gravel bed surfaces: Linking morphology to sediment transport processes and hydraulics. Sedimentology **56 (7) :** 2024-2043.

Hooke JM. 2003.Coarse sediment connectivity in river channel systems: a conceptual framework and methodology. Geomorphology **56** : 79-94.

Jerolmack DJ. 2011, Causes and effects of noise in landscape dynamics. Eos Trans. AGU, **92(44)** : 385. doi:10.1029/2011EO440001.

Jones JI, Collins AL, Naden PS, Sear DA. 2011 The relationship between fine sediment and macrophytes in rivers. River Research and Applications : published online. DOI: 10.1002/rra.1486.

Johnson MF, Reid I, Rice SP, Wood PJ. 2009. Stabilisation of fine gravels by net-spinning caddis fly larvae. Earth Surface Processes and Landforms **34** : 413-423.

Johnson MF, Rice SP, and Reid I. 2010 Topographic disturbance of subaqueous gravel substrates by signal crayfish (*Pacifastacus leniusculus*). Geomorphology **123** : 269 - 278.

Johnston CE, Andrews ED, Pitlick J. 1998. *In situ* determination of particle friction angles of fluvial gravels. Water Resources Research **34(8)** : 2017-2030.

Kean JW, Smith JD. 2006. Form drag in rivers due to small-scale natural topographic features: 1. Regular sequences. Journal of Geophysical Research-Earth Surface **111** : F04009.

Keller EA. 1971. Areal sorting of bed material: the hypothesis of velocity reversal. Geological Society of America, Bulletin **83**: 915–918.

Kemp P, Sear DA, Collins AL, Naden, PS, Jones JI. 2011. The impacts of fine sediment on riverine fish. Hydrological Processes **25(10)** : published online .DOI: 10.1002/hyp.7940.

Kirchner, JW, Dietrich, WE, Iseya, F and Ikeda, H. (1990) The variability of critical shear stress, friction angle and grain protrusion in water-worked sediments, Sedimentology **37** : 647-672.

Komar PD, Li Z. 1986 Pivoting analysis of the selective entrainment of sediments by size and shape with application to gravel thresholds. Sedimentology **33** : 425-436.

Lane SN, Bradbrook KF, Richards KS, Biron PM, Roy AG. 1999. The application of computational fluid dynamics to natural river channels: three-dimensional versus two-dimensional approaches. Geomorphology **29** : 1-20.

Lisle TE. 1989. Sediment transport and resulting deposition in spawning gravels, north coastal California.Water Resources Research **25** : 1303–1319.

MacWilliams MLJr, Wheaton JM, Pasternack GB, Street RL, Kitanidis PK. 2006. Flow convergence and routing hypothesis for riffle-pool maintenance in alluvial rivers. Water Resources Research **42** : W10427. DOI: 10.1029/2005WR004391.

McEwan I, Sørensen M, Heald J, Tait S, Cunningham G, Goring D, Willetts B. 2004. Probabilistic modelling of bed-load composition. Journal of Hydraulic Engineering **130 (2)** : 129-139.

Milan DJ, Heritage GL, Large ARG, Charlton ME. 2001 Stage-dependant variability in shear stress distribution through riffle-pool sequences. Catena **44** : 85-109.

Milne JA. 1982. Bed-material size and the riffle-pool sequence. Sedimentology **29** : 267-278.

Mosteller F, Tukey JW. 1977. Data analysis and regression: a second course in statistics. Addison-Wasley Publishing Company.

Oldmeadow DF, Church M. 2006. A field experiment on riverbed stabilisation by gravel structures. Geomorphology **78**: 335–350.

Pasternack GB, Gilbert AT, Wheaton JM, Buckland EM. 2006. Error Propagation for Velocity and Shear Stress Prediction: Using 2D Models For Environmental Management. Journal of Hydrology **328 (1-2)** : 227-241. DOI: 10.1016/j.jhydrol.2005.12.003.

Reid I, Frostick LE and Brayshaw AC. 1992. Microform roughness elements and the selective entrainment and entrapment of particles in gravel-bed rivers. In Dynamics of gravel-bed rivers, Billi P, Hey RD, Thorne CR, Tacconi P (eds.), John Wiley and Son Ltd, Chichester, 253-275.

Rice SP, Church M. 2010. Grain size sorting within river bars in relation to downstream fining along a wandering channel. Sedimentology **57** : 232-251.

Robert, A. 1990. Boundary roughness in coarse-grained channels. Progress in Physical Geography **14** : 42-70.

Schmeeckle MW, Nelson JM. 2003. Direct numerical simulation of bedload transport using a local, dynamic boundary condition. Sedimentology **50** 279 – 301.

Sear, D.A. 1992. Impact of hydroelectric power releases on sediment transport in riffle-pool sequences, in Billi, P., Hey, R.D., Thorne, C.R. & Tacconi, P. (eds.) Dynamics of Grabel-bed rivers, J.Wiley & Sons, Chichester, UK, 629-649..

Sear DA. 1996. Sediment transport processes in riffle-pool sequences. Earth Surface Processes & Landforms **21(3)** : 241-262.

Sear DA, Frostick LB, Rollinson G, Lisle TE. 2008. The significance and mechanics of fine sediment infiltration and accumulation in gravel spawning beds. In Salmonid Spawning habitat in Rivers; Physical controls, biological responses and approaches to remediation, Sear DA, DeVries P (eds.), AFS, Bethesda, Maryland, USA, 149-174.

Smart G, Aberle J, Duncan M, Walsh J. 2004. Measurement and analysis of alluvial bed roughness. Journal Of Hydraulic Research **42(3)** : 227-237.

Storey RG, Howard KWF, Williams DD. 2003. Factors controlling riffle-scale hyporheic exchange flows and their seasonal changes in a gaining stream: a three dimensional groundwater flow model. Water Resources Research **39** : 1034.

Sylte TL, Fischenich JC. 2002. Techniques for measuring substrate embeddedness. EMRRP Technical Notes Collection (ERDC TN-ENRRP-SR-36), U.S. Army Engineer Research and Development Center, Vicksburg, MS.

Tonina D, Buffington, JM. 2007. Hyporheic exchange in gravel bed rivers with pool-riffle morphology: Laboratory experiments and three-dimensional modeling.Water Resources Research **43** : W01421.

Vericat D, Batalla RJ, Gibbins C. 2008. Sediment entrainment and depletion from patches of fine material in a gravel-bed river. Water Resources Research **44** : W11415.

Wiberg PL, Smith JD. 1985. A theoretical model for saltating grains in water. Journal of Geophysical Research **90** : 7341-7354.

Whiting PJ and Dietrich WE. 1990. Boundary shear stress and roughness over mobile alluvial beds. Am. Soc. Civ. Eng. J. Hydraul., **116 (12)** : 1495-1511.

Figures

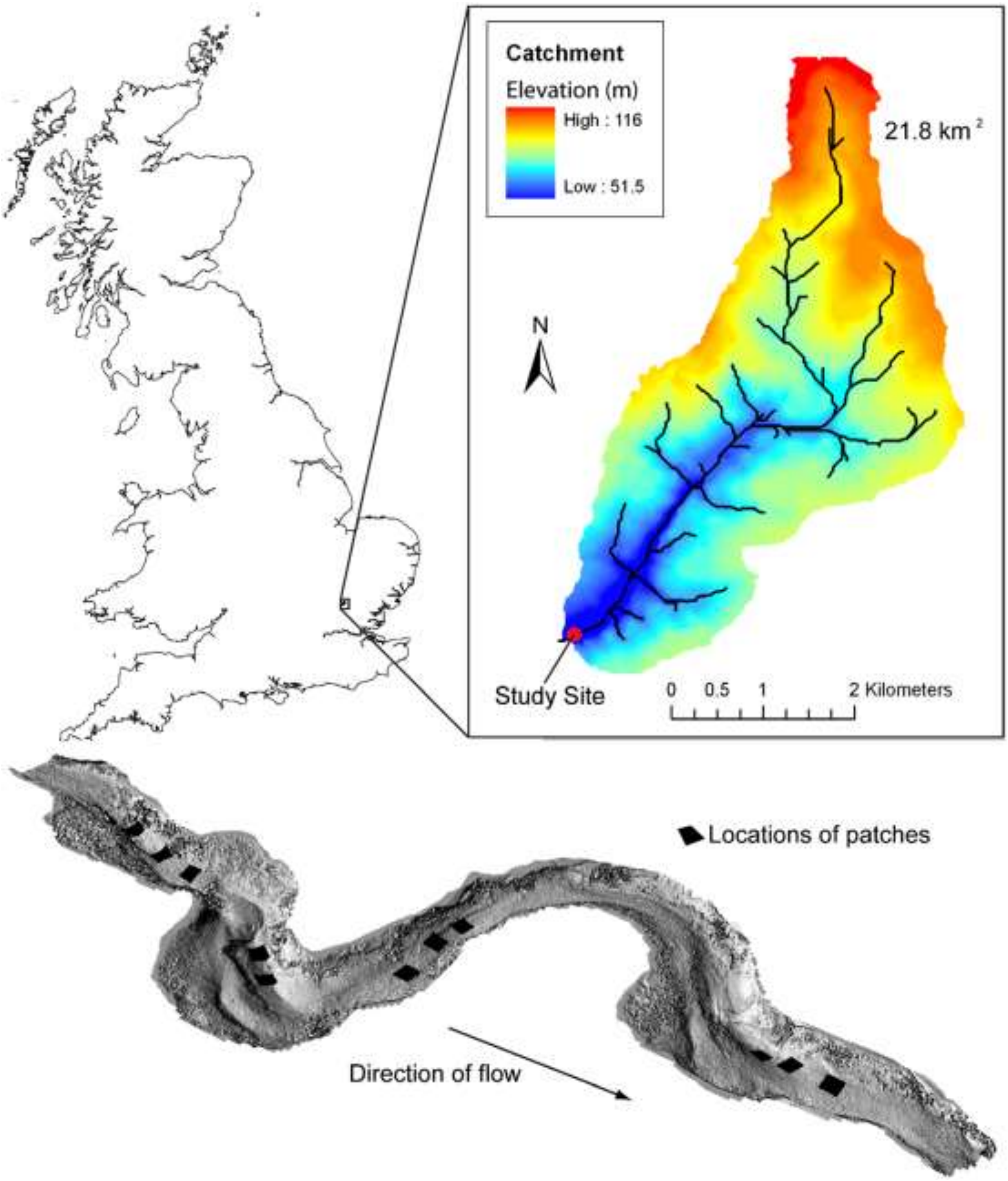

Figure 1: Location and topography of the 21.8 km^2 Bury Green Brook catchment in Essex, UK. Lower figure shows the study site reach of approximately 80 m (along thalweg) and the locations of the 1 m x 1 m patches which were scanned at high resolution. This figure is available in colour online.

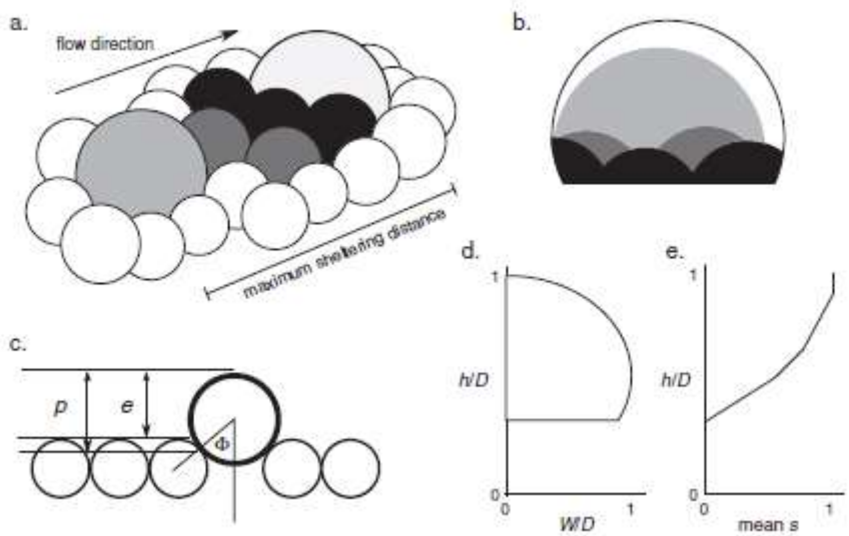

Figure 2: Methods of measuring grain exposure: a) Diagram showing grain for which exposure is being measured (white, thick outline) and sheltering grains. Sheltering grains are shaded according to their upstream distance relative to the maximum sheltering distance; darker grains exert a larger sheltering effect than lighter grains and white grains have no impact. b) Face of grain shaded according to upstream distance of sheltering grain, i.e. the value of weighting *s*. White areas have no shelter ($s = 1$), whereas black areas are highly sheltered ($s \sim 0$). c) 1D measurements of grain protrusion (p) and exposure (e). d) Variation in the width (W) of the exposed grain in (b) with height below the top of the grain (h). W and h are normalised by grain diameter (D). e) Variation in the width-averaged sheltering value (s) on the grain face in (b) with height. Sheltering varies from 1 (complete exposure over the maximum sheltering distance) to 0 (area of the grain is in contact with sheltering grains).

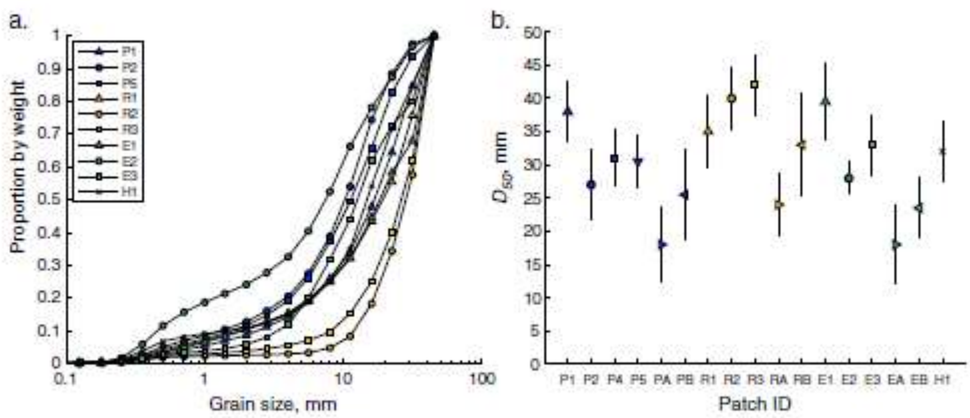

Figure 3: a) GSD of the surface layer of each 2009 patch (except P4), expressed as the weight of size fractions of a sifted surface sample. b) D_{50} of the coarse fraction of all 2006 and 2009 patches, calculated from all grains used for pivoting and lift measurements. Grains were selected using a grid. 95% error bars are also shown; error bars are calculated from the standard error of the median (Mosteller and Tukey, 1977) as $D_{50} \pm 1.253 \times 1.96 \times (\sigma/\sqrt{n})$, where σ is the standard deviation and n is the number of grains. This figure is available in colour online.

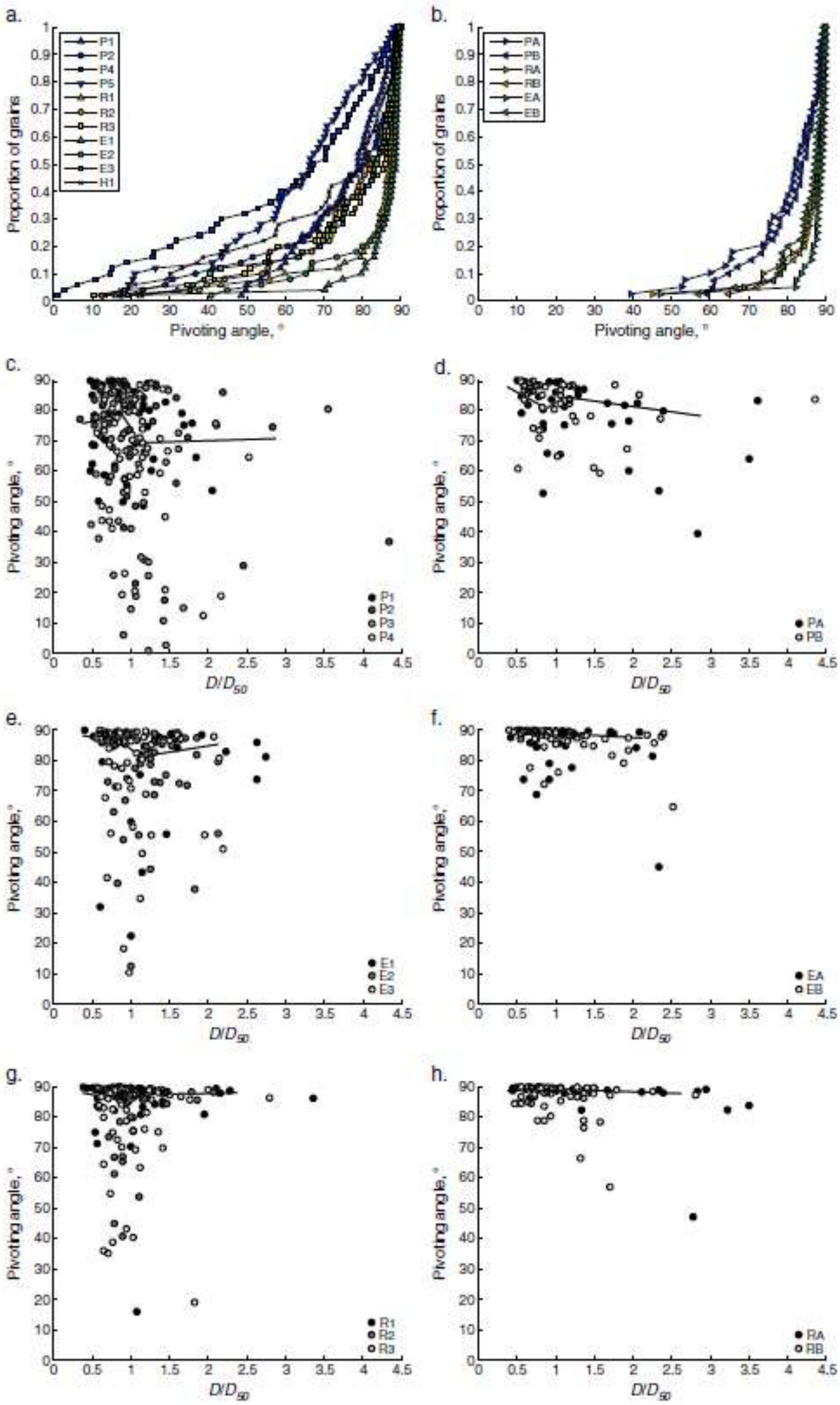

Figure 4: a and b) Cumulative distributions of grain pivoting angles from all patches from (a) 2009 and (b) 2006. c to h) Distributions of grain pivoting angles as a function

of grain b-axis length. Data are from (c and d) pools, (e and f) pool exits and (g and h) riffles. Data are from (c, e and g) 2009 and (d, f and h) 2006. Within each subplot, data points are shaded according to which patch they were measured from. The line shows the 50th percentile fitted to grain size bins containing at least 30 grains. This figure is available in colour online.

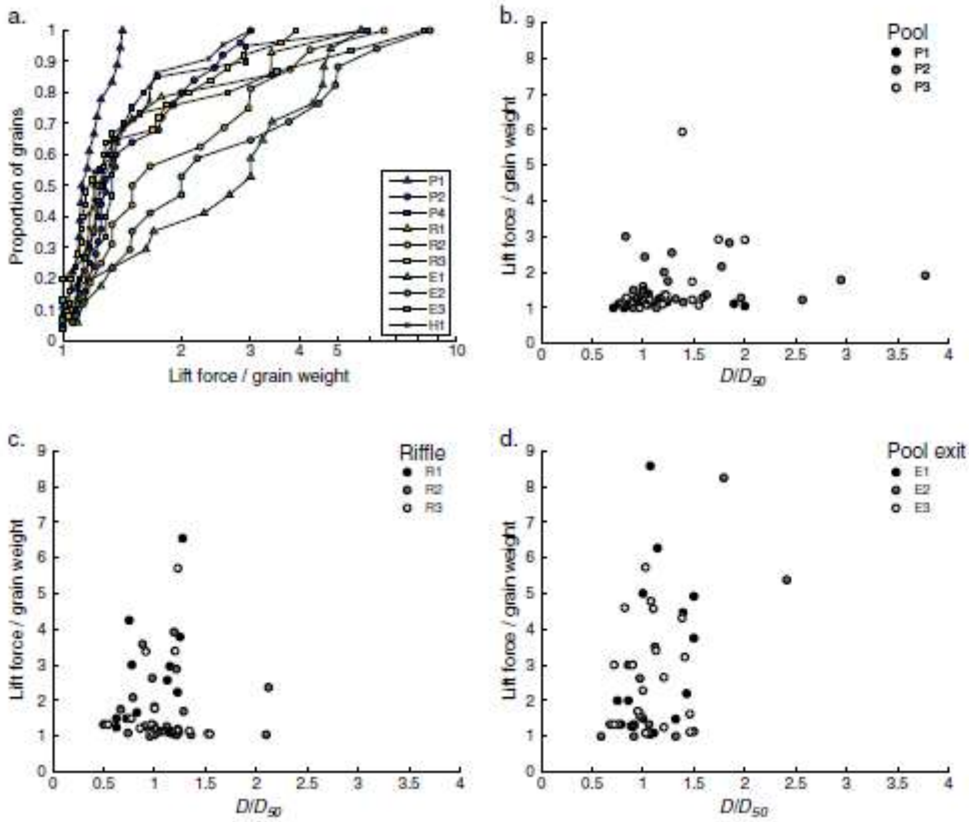

Figure 5: a) Cumulative distributions of lift force per unit grain weight, *m*, for the different patches. b – d) Distributions of *m* as a function of D/D_{50} for the different facies. Different patches are plotted in different shades. This figure is available in colour online.

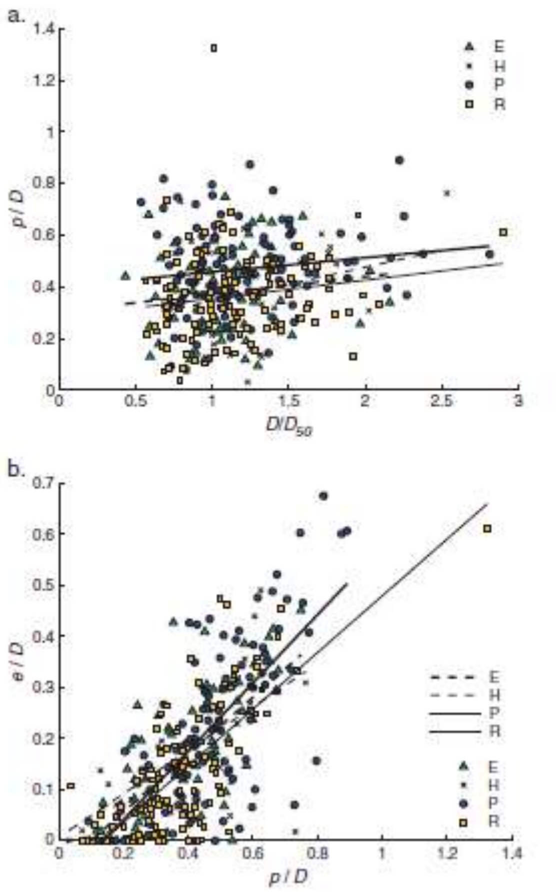

Figure 6: a) Relationship between relative protrusion (p/D) and D/D_{50}. b) Relationship between relative exposure (e/D) and p/D. Linear regression lines are fitted to each dataset. This figure is available in colour online.

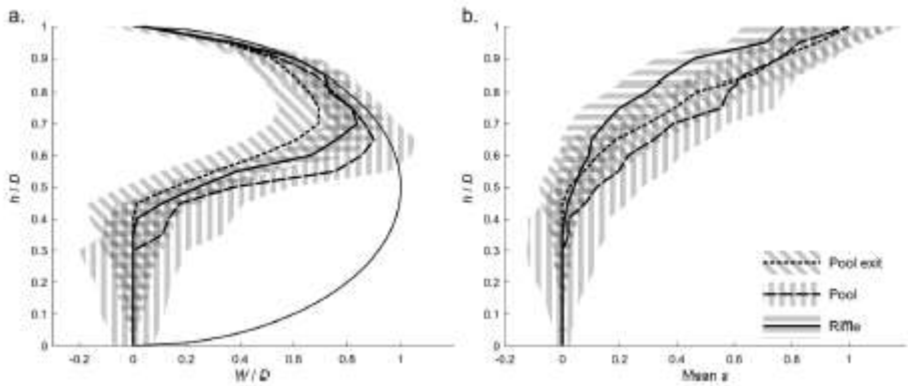

Figure 7: a) Median distributions of grain exposure width (W/D) as a function of elevation (h/D). For each value of h/D, the plotted value of W/D is the median of W/D for all grains from that facies. Black thin line shows W/D for a completely exposed sphere. b) Median distributions of sheltering weighting (s) as a function of h/D. For

each grain, s is initially calculated as the mean s across the grain at each value of h/D. This plot shows the median of the mean values from all grains within a facies. Both plots show data from pool, pool exit and riffle facies. 95 % error bands around the median are calculated as 1.96 × standard error of the median.

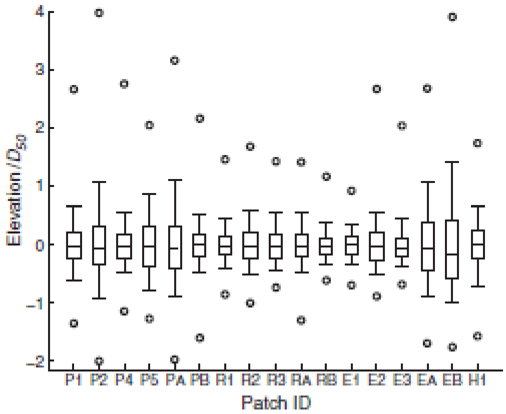

Figure 8: Distributions of surface elevations from all patches. Boxplots show the 25th to 75th percentiles, dashed line is the median, whiskers show the 5th to 95th percentiles and circles show the maximum and minimum. All elevations are normalised by the patch D_{50} (in Figure 3b), and all patches have a mean elevation of 0.

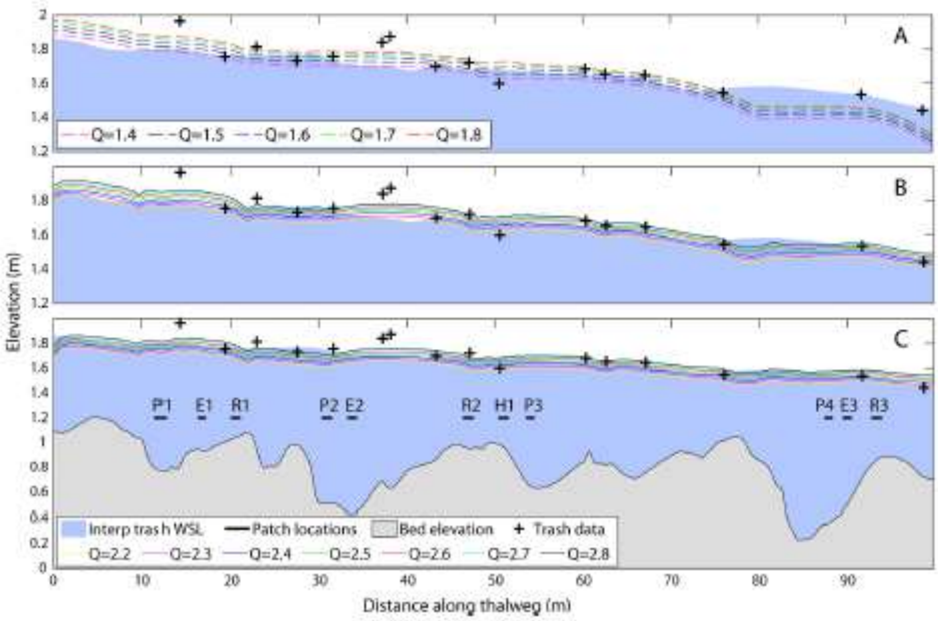

Figure 9: Channel topography along the thalweg of the reach, showing location of patches. The water surface interpolated from the trash markers is shown in blue, and

the trash marks as crosses. Water surfaces modelled using Hydro2de and discharges between 2.2 and 2.8 m^3s^{-1} are shown for A) low and B) standard Manning's n parameterisations. For C) high Manning's n parameterisations discharges between 1.4 and 1.8 m^3s^{-1} are shown. Best fits are given by 2.6 m^3s^{-1} (low n) and 2.5 m^3s^{-1} (standard n). This figure is available in colour online.

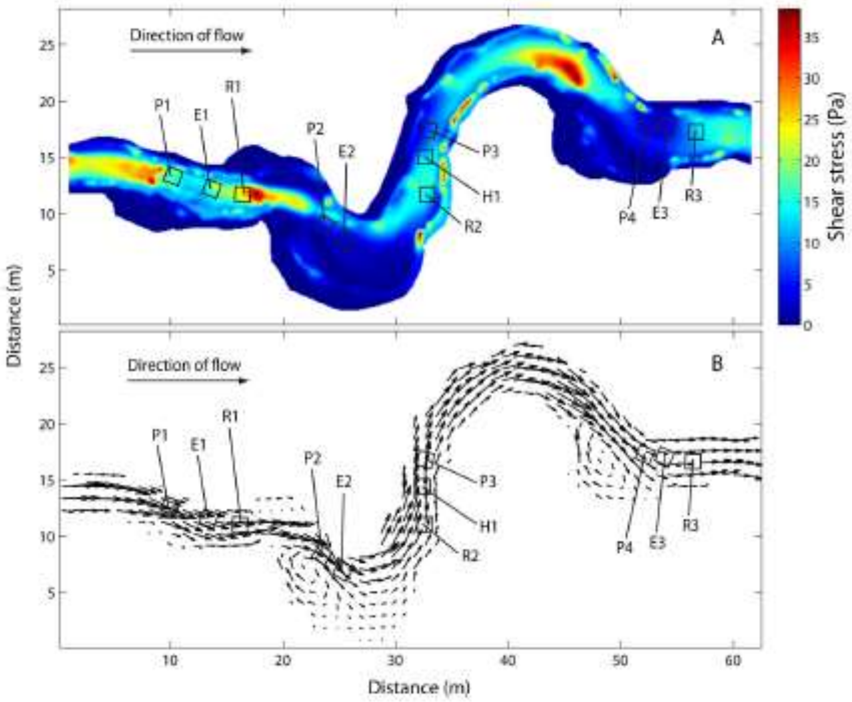

Figure 10: The spatial distribution of shear stress and flow velocity in a model run with standard n and a discharge of 2.5 m^3s^{-1}. Note the unidirectional and relatively faster flow over the riffles. Squares show locations of field measurements. This figure is available in colour online.

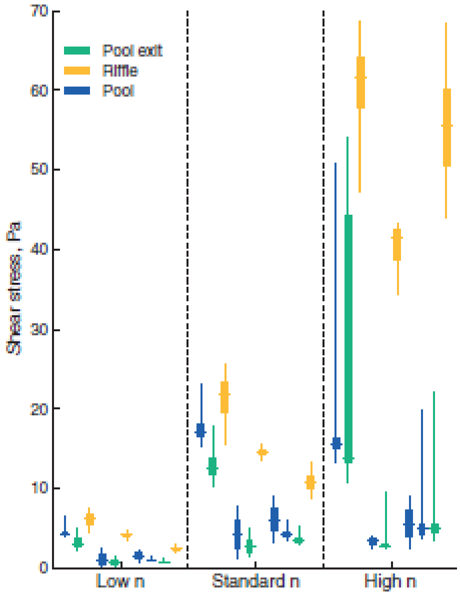

Figure 11: Distributions of shear stress across patches under different parameterisations of Manning’s n. For each parameterisation the discharge shown is that which best reproduces the trash surface (low n, Q = 2.6 m^3s^{-1}; standard n, Q = 2.5 m^3s^{-1}; high n, Q = 1.5 m^3s^{-1}). Each distribution represents the range of shear stress from a single patch (thin line shows minimum to maximum, thick line shows interquartile range and horizontal line shows the median). For each paramerisation patches are plotted from left to right in the downstream order (P1, E1, R1, P2, E2, R2, P3, P4, E3, R3). This figure is available in colour online.

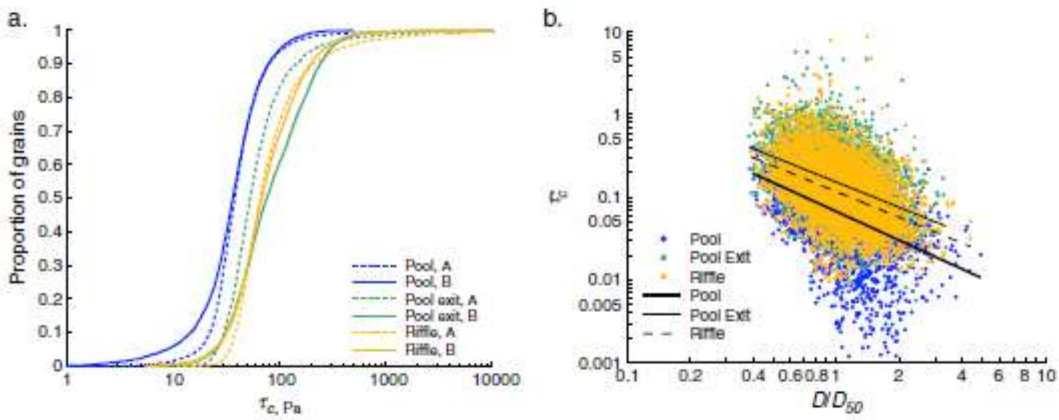

Figure 12: a) Distributions of critical entrainment shear stress (τ_c) for grains in pool, pool exit and riffle facies, as predicted by grain entrainment model runs A and B. See

text for model descriptions. b) Relationship between D/D_{50} and τ_c* for grains from model B runs with pool, pool exit and riffle parameter values. Linear regressions have equations: pool grains, [illegible]; pool exit grains, [illegible]; riffle grains, [illegible]. p-values for all regressions are < 0.0001, and the gradient for the pool exit and riffle regressions are not significantly different to -1 (α=0.05).This figure is available in colour online.

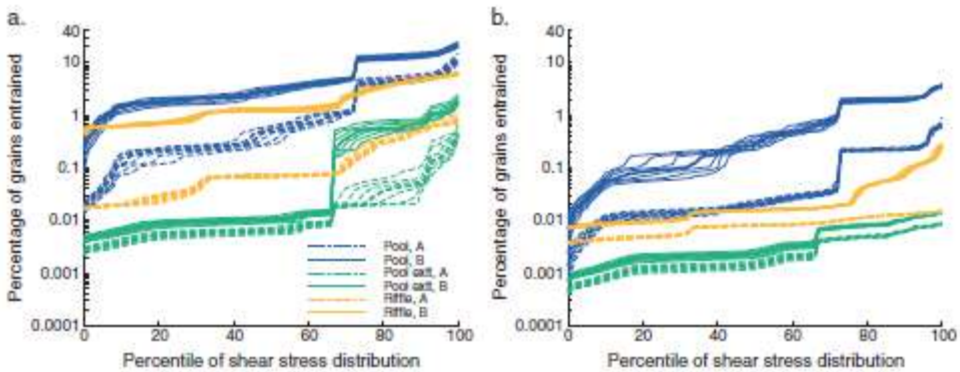

Figure 13: Comparison between the distributions of critical entrainment shear stress (τ_c) predicted from the field data and the distributions of shear stress predicted by the CFD model using a) standard and b) low parameterisation of Manning's n. Each plot shows the percentage of grains that would be entrained by different percentiles of the CFD shear stress distribution. Distributions of τ_c are predicted for grains in pool, pool exit and riffle facies using both models A and B. Results are shown for all seven discharges used in the flow model; the bold line shows the optimum discharge. This figure is available in colour online.

Tables

Table 1: Parameters needed for the grain entrainment model, and the methods used to derive parameter values from the field data. Only the 2009 data are used. (A) and (B) refer to the two model variants.

Parameter	Method	Parameter values
Grain diameter (*D*)	Random sampling from lognormal fit to patch GSDs. Equal proportion of grains are selected from each patch within the facies.	Mean/variance of lognormal distribution (mm) Pool: 38/221, 32/243, 34/150, 32/109 Pool exit: 41/322, 29/59, 37/180 Riffle: 40/293, 44/253, 46/223
D_{50}/D_{84}	Taken from same patch as *D*	D_{50}/D_{84} (mm) Pool: 38/51, 27/46, 31/45, 30.5/42 Pool exit: 39.5/57, 28/37, 33/50 Riffle: 35/55, 40/58, 42/60
Pivoting angle (Φ)	Identify size class for grain (D/D_{50}, as in Figure 4), randomly select percentile (*n*), and interpolate value of Φ for that percentile from field data	Percentile distributions as in Figure 4.
Lift force multiple (*m*)	(A) Resistance to lift not included (B) Randomly select percentile, and interpolate that percentile from distribution of all values of *m* from that facies.	$m = 1$ Use distributions in Figure 5
Grain protrusion (*p*)	(A) Randomly sample from normal distribution fitted to the field data from that facies (B) 100-n^{th} percentile of normal distribution fitted to field data	Mean/standard deviation of normal distribution (-) Pool: 0.47/0.17 Pool exit: 0.38/0.16 Riffle: 0.37/0.17
Grain exposure (*e*)	Calculated from the regression between *p*/*D* and *e*/*D*, with normally distributed errors *E*: $e/D = a\ p/D + b + E$	*a*/*b*/standard deviation of *E* (-) Pool: 0.67/-0.09/0.11 Pool exit: 0.56/-0.06/0.09 Riffle: 0.56/-0.08/0.09

Table 2: Summary of trends in field measurements and DTM analysis

Bedform		Riffle	Pool head	Pool	Pool exit
Grain size	Trend	Larger	Smaller	Smaller	Intermediate
	D_{50} (mm)	35 - 42	32	27 - 38	28 - 37
	Sear (1996)	*Largest*			*Smallest*
Pivoting angle	Trend	High	Intermediate	Low	Highest
	Φ (°)[a]	76	70	62	83
Lift force	Trend	Intermediate	Low	Low	High
	mean m (F_L/F_W)	1.9	1.6	1.5	2.7
Grain exposure	Trend (*W/D*):	Intermediate	n/a	High	Low
	Trend (s):	High	n/a	Low	Intermediate
	Sear (1996)	*Low*			*High*
Surface roughness	Trend	Low	Intermediate	High	Low
	Range/D_{50}	0.73 – 1.10	1.36	0.99 – 2.01	0.72 – 1.08
Entrainment shear stress	Trend	High	n/a	Low	High
	median τ_c (Pa)[b]	68.1	n/a	36.2	77.4
	Sear (1996)	*High*			*Low*

[a]Pivot angle predicted for $D/D_{50} = 1$ from fit of equation 10 to the data.

[b]Predicted using model B.